Article:
Veneri, Alessandro, Rappoport, Tatiana G. and Ferreira, Aires (2025) Extrinsic Orbital Hall Effect: Orbital Skew Scattering and Crossover between Diffusive and Intrinsic Orbital Transport. Physical Review Letters. 136201. ISSN: 1079-7114

https://doi.org/10.1103/PhysRevLett.134.136201

Extrinsic Orbital Hall Effect: Orbital Skew Scattering and Crossover Between Diffusive and Intrinsic Orbital Transport

Alessandro Veneri,[1] Tatiana G. Rappoport,[2,3] and Aires Ferreira[1,*]

[1] *School of Physics, Engineering and Technology and York Centre for Quantum Technologies, University of York, York YO10 5DD, United Kingdom*

[2] *Physics Center of Minho and Porto Universities (CF-UM-UP),Campus of Gualtar, 4710-057, Braga, Portugal*

[3] *International Iberian Nanotechnology Laboratory (INL), Av. Mestre José Veiga, 4715-330 Braga, Portugal*

Despite the recent success of identifying experimental signatures of the orbital Hall effect (OHE), the research on the microscopic mechanisms behind this unique phenomenon is still in its infancy. Here, using a gapped 2D Dirac material as a model system of the OHE, we develop a microscopic theory of orbital transport which captures extrinsic disorder effects non-perturbatively. We show that it predicts several hitherto unknown effects, including (i) a strong dependence of the orbital Hall conductivity with the strength and symmetry of the impurity scattering potential, and (ii) a smooth crossover from intrinsic to extrinsic OHE as a function of the Fermi energy and impurity density. In contrast to previous (perturbative) studies, the OHE is found to exhibit bona fide diffusive behavior in the dilute impurity limit, which we trace back to the dominance of skew scattering-type processes. More generally, we argue that the newly unveiled orbital skew scattering mechanism governs the diffusive OHEs of a large class of 2D materials even when the crystal structure is inversion-symmetric. Our work unveils the crucial nature of non-perturbative vertex corrections for a complete description of orbital transport and confirms common short-range impurities as key enablers of the OHE.

The transport of orbital angular momentum (OAM) in solids has garnered significant interest for its fundamental role in understanding quantum dynamics in spin-orbit coupled systems and its potential for device applications [1–4]. In materials with weak spin-orbit coupling, charge-neutral orbital currents can be generated electrically via the orbital Hall effect (OHE) [5–7], first proposed in 2005 [8] and recently observed in experiments on light metals [9–11]. This development is steering spintronics in new directions, with studies addressing orbital torques, ultrafast OAM transport, and more [12–26].

Efforts to unravel the microscopic mechanisms of the OHE have primarily focused on intrinsic transport driven by momentum-space orbital textures, often linked to quantum geometric effects [27]. However, theoretical estimates based solely on intrinsic mechanisms differ significantly from experimental results in titanium thin films, suggesting that disorder plays a critical role in the relaxation of nonequilibrium orbital densities [9]. Recent theoretical work supports this view, showing that thermal disorder at room temperature is an important piece of the OHE puzzle [28–30]. A pressing challenge moving forward is to understand how disorder, particularly short-range defects and impurities, affect the generation of OAM currents. Short-range defects are ubiquitous in metals and other OHE candidate materials [11] and may enable efficient mechanisms of extrinsic orbital transport. A strong contender, hitherto unconsidered, is orbital skew scattering (i.e. the orbital analog of Mott scattering), whereby an applied electric field causes wave packets with opposite OAM (e.g., $L_z = \pm\hbar$) to scatter asymmetrically, resulting in transverse OAM flow. Two such mechanisms may contribute to the OHE without the need for spin-orbit coupling: (i) asymmetric scattering due to impurities with non-trivial orbital-space structure, and (ii) asymmetric scattering enabled by the orbital texture of wavefunctions. The former may induce OHE in otherwise orbital-inactive systems, while the latter is a band-driven mechanism whose spin analog has been found to emerge in 2D materials with broken spatial symmetries [31, 32].

Despite the increasing interest surrounding the OHE, only a few studies have systematically examined the role of disorder [33–37]. Although a coherent picture has not yet emerged, this early work suggests that a non-perturbative treatment of disorder at some level of theory will be crucial to unlock the extrinsic OHE. Our purpose in this Letter is to fill this gap. The key issue concerns the exact nature of the vertex corrections to the orbital Hall conductivity (OHC). Specifically, Ref. [34] predicts an extrinsic OHE insensitive to the disorder parameters, while Ref. [36] finds that vertex corrections of the OHC vanish entirely for short-range impurities. In contrast, numerical real-space calculations carried out for small system sizes clearly show a disorder-dependent OHE [37]. Although real space numerics can simulate tight-binding models of arbitrary complexity [38], reaching the interesting diffusive regime of macroscopic systems at low impurity densities remains a considerable challenge [39]. Here, diagrammatic linear-response techniques can prove

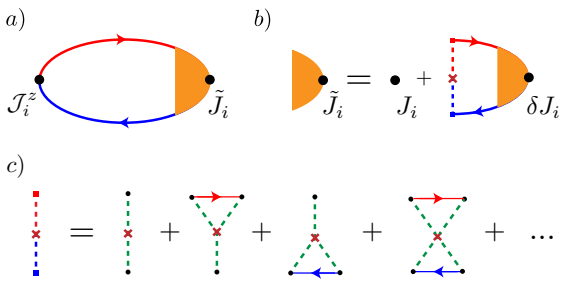

FIG. 1. Diagrammatic technique: (a) the extrinsic OHC; (b) the disorder-renormalized charge current vertex function; and (c) the T-matrix expansion of this work. In the popular ladder approximation, only the first diagram in (c) is retained. This captures side-jump processes perturbatively, but misses out the skew scattering mechanism as well as the strong scattering regime. Solid (dashed) lines denote disorder-averaged Green's function (single-impurity potential insertions), while red/blue indicates advanced/retarded sectors.

exceedingly useful, as they capture the diffusive regime by design. Indeed, we will show below that a formulation beyond the standard perturbative approach solves the conundrum of the vertex corrections and unveils a rich OHE phenomenology, where the microscopic details of the disorder landscape occupy the center stage.

Setting the stage. —We explore a system of massive 2D Dirac electrons, a prototypical model for 2D materials with broken inversion symmetry. We note, however, that the extrinsic OHE and its main driving force (see below) are expected to be universal features of a large class of orbital-active 2D materials, including centrosymmetric systems. Orbital physics in 2D materials [40–49] such as dichalcogenide monolayers, has previously been linked to phenomena like orbital Hall insulating phases [41, 44] and OAM-carrying in-gap edge states [50]. To incorporate disorder into the picture, we employ a diagrammatic technique wherein electron-impurity scattering events responsible for vertex corrections to the OHC are described via a *generalized ladder* series of Feynman diagrams [51]. It accomplishes the exact resummation of the infinite series of 2-particle non-crossing diagrams ("ladder", "Y", "X", etc.; see Fig. 1). Hence, all the extrinsic mechanisms triggered by single-impurity scattering events (e.g., semiclassical skew scattering, asymmetric scattering precession [52] and side jumps) are captured in a *fully nonperturbative* fashion [51]. Previous applications include the spin Hall effect (SHE) in twisted 2D heterostructures [32] and the anomalous Hall effect in magnetized 2D materials [53]. Armed with this formalism, we uncover the dominant OHE mechanisms (most notably, orbital skew scattering) and construct a phase diagram of OAM transport spanning extrinsic and intrinsic regimes. The crucial role played by the symmetry of the scattering centers will also be addressed.

Theory.—The single-particle Hamiltonian around the $K(K')$ point in the valley-isotropic basis reads as

$$H_\tau = v\,\boldsymbol{\sigma}\cdot\mathbf{p} + \tau\Delta\,\sigma_z + V_{\rm dis}(\mathbf{x}) \tag{1}$$

where v is the bare Fermi velocity of 2D massless Dirac fermions, $\mathbf{p} = -i\hbar\boldsymbol{\nabla}$ is the momentum operator, $\boldsymbol{\sigma}$ is the vector of pseudospin Pauli matrices and $\tau = \pm 1$ is the valley index. Moreover, Δ is a staggered on-site potential leading to an energy gap $E_g = 2\Delta$ and $V_{\rm dis}(\mathbf{x})$ describes the disorder landscape. To get a broader picture of the extrinsic OHE, here we shall consider a generalized short-range impurity model. Specifically, $V_{\rm dis}(\mathbf{x}) = \sum_i M_{\rm dis}(u_0, u_z)\,\delta(\mathbf{x}-\mathbf{x}_i)$, where $M_{\rm dis}(u_0, u_z) = u_0\,\sigma_0 + u_z\,\tau\sigma_z$, $\{\mathbf{x}_i\}$ is the set of impurity positions ($i = 1, ..., N$), $u_{0(z)}$ is the strength of the scalar (staggered) component of the scattering potential, and σ_0 is the 2×2 identity matrix. Our main quantum observable of interest is the orbital-current operator $\mathcal{J}_i^z = \frac{1}{2}\{j_i, L_z\}$, where $j_i = v\,\sigma_i$ (with $i = x, y$) is the particle current operator, L_z is the $\hat{z}$ component of the OAM operator and $\{\cdot,\cdot\}$ denotes the anticommutator. L_z has the following momentum-space representation in the valley-isotropic basis $L_z(\mathbf{k}) = -\hbar\,\sigma_0\tau\Delta m_e v^2/E_{\mathbf{k}}^2$ [45], where m_e is the electron mass, $E_{\mathbf{k}} = \sqrt{\hbar^2v^2k^2 + \Delta^2}$ is the energy dispersion, and $k = |\mathbf{k}|$ is the wavevector measured from a valley. We note that wavepackets centered at the K and K' points carry opposite OAM due to time-reversal ($\mathcal{T}$) symmetry. Because the impurity Hamiltonian in our model is diagonal in valley space (i.e. intervalley scattering terms are neglected), the total OHC is two times the OHC of a single valley. In the following, we work in the K-valley sector ($H \equiv H_{\tau=1}$) and introduce a valley degeneracy factor ($g_v = 2$) when required.

The extrinsic contribution to the linear-response OHC in the dilute impurity limit is governed by the Fermi-surface (type I) term of the Kubo-Streda formula:

$$\sigma_{ij}^{\rm OHE}(\varepsilon) = \frac{g_v g_s}{2\pi}\int d\mathbf{k}\,{\rm tr}\left[\mathcal{J}_i^z(\mathbf{k})\,\left\langle G_\varepsilon^+\,J_j\,G_\varepsilon^-\right\rangle(\mathbf{k})\right], \tag{2}$$

where $J_i = -ej_i$ is the charge current operator ($e > 0$), $G_\varepsilon^\pm = (\varepsilon - H \pm i0^+)^{-1}$ is the retarded(+)/advanced(−) Green's function at the Fermi energy ε, $g_s = 2$ is the spin-degeneracy factor, $\langle ...\rangle$ is the disorder average, $\hbar \equiv 1$, and the trace is taken over the pseudospin degree of freedom. The expression inside angular brackets can be cast as $\langle G_\varepsilon^+\,J_j\,G_\varepsilon^-\rangle \to \mathcal{G}_\varepsilon^+(\mathbf{k})\,\tilde{J}_j\,\mathcal{G}_\varepsilon^-(\mathbf{k}) \equiv 2\pi\varrho_j(\varepsilon,\mathbf{k})$, where $\mathcal{G}_\varepsilon^\pm(\mathbf{k})$ are disorder-averaged Green's functions and $\tilde{J}_j$ is the disorder-renormalized charge current operator obtained by solving the Bethe-Salpeter equation in Fig. 1(b). Explicitly, we have: $\mathcal{G}_\varepsilon^\pm(\mathbf{k}) = (\varepsilon - H_0(\mathbf{k}) - \Sigma_\varepsilon^\pm)^{-1}$, where $H_0(\mathbf{k})$ is the disorder-free Hamiltonian, $\Sigma_\varepsilon^\pm = n\,T^\pm(\varepsilon)$ is the disorder self-energy, $T^\pm(\varepsilon)$ is the single-impurity T matrix, and n is the impurity density in the thermodynamic limit ($N \to \infty$); see Ref. [54] for detailed

expressions of $\mathcal{G}^{\pm}_{\varepsilon}(\mathbf{k})$, $T^{\pm}(\varepsilon)$ and $\tilde{J}_j(\varepsilon)$. All together, the knowledge of the renormalized vertex yields the extrinsic OHC via $\sigma^{\rm OHE}_{ij}(\varepsilon) = g_s g_v \int d\mathbf{k}\, {\rm tr}\,[\mathcal{J}^z_i(\mathbf{k})\varrho_j(\varepsilon,\mathbf{k})]$. This elegant expression shows that $\varrho_j(\varepsilon,\mathbf{k})$ plays the role of a $\mathbf{k}$-resolved density matrix encapsulating the linear response of the system, and therefore that the *structure of the renormalized vertex is key* [54]. Finally, the intrinsic OHC, $\sigma^{\rm int}_{\rm OHE}$, is obtained by momentum space integration of the orbital Berry curvature [45]. In what follows, we assume that the electric field driving the OHE is applied along the $\hat{x}$ axis and define $\sigma^{\rm dis.}_{\rm OHE} \equiv \sigma^{\rm OHE}_{yx}$ (due to symmetry of the model, we also have $\sigma^{\rm OHE}_{xy} = -\sigma^{\rm OHE}_{yx}$).

Results and discussion.—We consider two types of scattering centers: (i) conventional scalar impurities and (ii) impurities with $u_z \neq 0$. Both cases are realistic and commonly realized. A simple example is a top impurity with C_{3v} symmetry (e.g. an ad-atom chemisorbed on an A- or B-type site in graphene [55–57]). Its localized nature around a site belonging to a particular sublattice (A or B) implies $u_z \approx \pm u_0$, so that the projection of $M_{\rm dis}$ on the opposite sublattice (B or A) vanishes or is strongly suppressed. In contrast, hollow-position impurities enjoy 6-fold rotational symmetry and thus generate purely scalar potentials ($u_z = 0$) [58]. This justifies our use of a generalized disorder model, and will allow us to draw a number of conclusions regarding the nature of possible OHEs. We first focus on scalar impurities, as they are the most symmetric ones. To help uncover the main driver of the extrinsic OHE, we expand Eq. (2) in powers of the n [or equivalently, $1/(\varepsilon\tau_0)$, where $\tau_0 \propto n^{-1}$ is a typical (charge) scattering time]. The leading term of the expansion $\mathcal{O}(n^{-1})$ encodes the semiclassical response:

$$\sigma^{\rm s.c.}_{\rm OHE} = \chi_\varepsilon \frac{2em_e v^2}{\pi n}\theta(|\varepsilon|-|\Delta|)\left[\frac{\Delta^2}{u_0\varepsilon^2}\frac{f_1(\varepsilon,\Delta)}{f_2(\varepsilon,\Delta)} + \frac{4\Delta^4 f_1(\varepsilon,\Delta)\log\left(\frac{\Lambda^2}{\varepsilon^2-\Delta^2}-1\right)}{\pi v^2\varepsilon\,[f_2(\Delta,\varepsilon)]^{3/2}} + \mathcal{O}(u_0)\right], \quad (3)$$

where $\chi_\varepsilon = {\rm sign}(\varepsilon)$, $f_1(\varepsilon,\Delta) = (\epsilon^2-\Delta^2)^2$, $f_2(\Delta,\varepsilon) = \left(\varepsilon^2+3\Delta^2\right)^2$, and $\Lambda \gg \varepsilon,\Delta$ is an energy cutoff used to regularize diverging integrals appearing at higher order (typically $\Lambda \approx 10$ eV, but the results are little sensitive to actual choice of Λ [59]). The validity of the analytical u_0-expanded result [Eq. (3)] (accurate for $|u_0|$ up to ≈ 0.2 eV nm^2) is discussed in the Supplemental Material [54].

The first term of Eq. (3) is inversely proportional to the potential strength and has odd parity, i.e. $\sigma^{\rm s.c.}_{\rm OHE}(\varepsilon) = -\sigma^{\rm s.c.}_{\rm OHE}(-\varepsilon)$, unlike $\sigma^{\rm int}_{\rm OHE}$ which is an even function of ε [45]. This symmetry is perturbatively broken due to disorder, and, for intermediate scattering strengths, an important next-order contribution [the second term in Eq.(3)] kicks in. This effect can be seen in Fig. 2, where the total OHC, $\sigma^{\rm tot}_{\rm OHE} = \sigma^{\rm dis.}_{\rm OHE} + \sigma^{\rm int.}_{\rm OHE}$, is

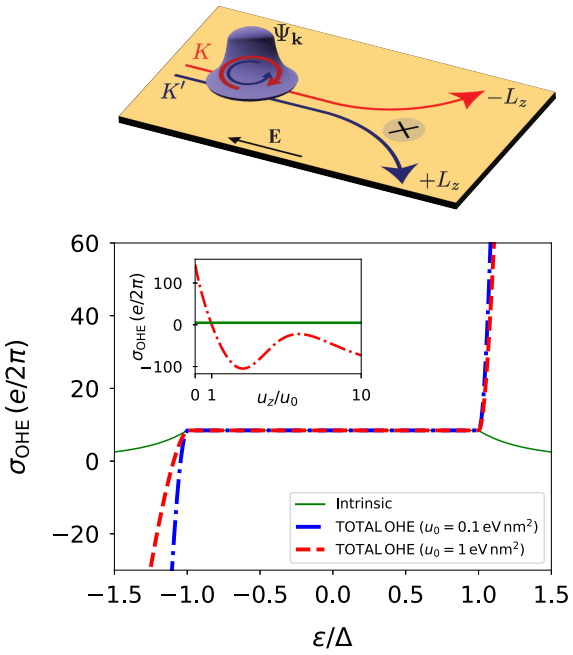

FIG. 2. Top panel: Illustration of the orbital skew scattering mechanism leading to a transverse net flow of OAM. Bottom panel: Fermi energy dependence of the total OHC ($\sigma^{\rm tot}_{\rm OHE} = \sigma_{\rm OHE} + \sigma^{\rm int}_{\rm OHE}$) in the presence of dilute random impurities for selected scalar potential strengths. Inset: Extrinsic OHC as a function of u_z/u_0 for $\varepsilon = 1.2\Delta$ (note that $|\sigma^{\rm int}_{\rm OHE}|$ is shown as a solid line for comparison). Parameters: $v = 10^6$ m/s, $\Delta = 0.5$ eV, $n = 10^{12}$ cm^{-2}, and $u_0 = 1$ eV nm^2 (inset).

plotted against the Fermi energy for two choices of u_0 and a fixed n. We note that $\sigma^{\rm dis.}_{\rm OHE}$ matches well the analytical approximation of Eq. (3) in this low-u_0 regime. The extrinsic OHC is seen to depend strongly on u_0 and in the metallic regime it can *easily exceed* $\sigma^{\rm int.}_{\rm OHE}$, especially for low n. To understand this behavior, one needs to pin down the exact underlying mechanism of the extrinsic response. The sensitivity of $\sigma^{\rm dis.}_{\rm OHE}$ to the impurity potential strength suggests that an orbital version of the familiar (spin-dependent) skew scattering mechanism is at play. To confirm this, we also perform a standard ladder resummation. The rationale is that, by construction, the ladder approximation excludes semiclassical skew-scattering diagrams (most notably the Y diagram [51]). We find $\sigma^{\rm ladder}_{\rm OHE} = 0$ (to the leading order in n), which confirms our hypothesis. Due to the semiclassical nature of the skew scattering mechanism, one has $\sigma_{\rm OHE} \sim n^{-1}$ akin to the familiar Drude conductivity (σ_{xx}). However, the transport times governing each response function are drastically different. To leading order in u_0, one has $\sigma^{\rm s.c.}_{\rm OHE}(\varepsilon) \propto (n\varepsilon^2 u_0)^{-1}$, while $\sigma_{xx}(\varepsilon) \propto \varepsilon\tau_{\parallel}$ with $\tau_{\parallel} \propto (n\varepsilon u_0^2)^{-1}$ (here, the high Fermi energy limit $\varepsilon \gg \Delta$ was taken for simplicity). This shows that, in analogy to the extrinsic SHE, the *orbital-*

Hall response is governed by its own transverse transport time, namely, $\sigma^{\rm s.c.}_{\rm OHE} \propto v k_F \tau_\perp$, with $k_F = \sqrt{f_1(\varepsilon,\Delta)}$ [the parametric dependencies of $\tau_\perp$ can be read off from Eq. (3)]. Due to $\mathcal{T}$ symmetry, the skewness of impurity cross sections features a *valley-orbit locking effect* akin to the intrinsic OHE mechanism [45]; see Fig. 2 (top panel).

The characteristic behavior of the OHC reflects the structure of the disorder-renormalized vertex $\tilde{J}_x$. We find $\tilde{J}_x = a\, J_x + b\, J_y$, with a, b some $\mathcal{O}(n^0)$ constants [54]. The $\mathcal{O}(n^0)$ J_y term (absent in the ladder approximation) shows that, through skew scattering, disorder acts as a robust source of transverse OAM flow (note that $\mathcal{J}^z_y \propto J_y$ in our model). Moreover, the nonperturbative dependence of $\tilde{J}_x$ on the scattering potentials u_0 and u_z is accessible via our technique [54]. It is instructive to compare our findings to Ref. [34], where a white-noise (WN) model of scalar disorder was employed. There, the leading term of the small-n expansion reads $\sigma^{\rm WN}_{\rm OHE} \propto (n)^0$, suggesting that a noncrossing calculation is insufficient (see Refs. [51, 60] for a discussion of the breakdown of perturbative analysis in 2D Dirac models with WN and similar zero-spatial-average disorder landscapes). The WN statistics yield an extrinsic OHC *independent* on the disorder details, as well as an unphysical C_0-type discontinuity as the Fermi energy approaches the band edge [34]. In contrast, in our model (of random short-range impurities), the extrinsic OHC shows regular behavior across the band edge and the semiclassical skew scattering mechanism is operative ($\sigma^{\rm s.c.}_{\rm OHE} \propto n^{-1}$), leading to a physically sound $\sigma^{\rm dis.}_{\rm OHE}$ that is sensitive to u_0 and n as expected in a realistic disordered material.

It is natural to ask whether the intrinsic mechanism can prevail over orbital skew scattering in the regime of diffusive charge transport. To answer this question, we performed a detailed study in the parameter space spanned by ε and the orbital mass of the gapped 2D Dirac model. Note that the low native defect concentrations [61] of graphene implies that, in this system (where a sizable Δ can be induced via strain fields [62, 63]), skew scattering is expected to dominate the OAM transport. For this reason, we shall focus on the case of transition metal dichalcogenide (TMD) monolayers. Here, the area density of point defects can reach a few $10^{13}\,\mathrm{cm}^{-2}$ [64, 65], taking the system closer to the actual "dirty limit". To establish a physical picture, we map out the relative contribution of the skew scattering-driven OHE, $\eta_{\rm dis} \equiv \bar{\sigma}^{\rm dis}_{\rm OHE}/(\bar{\sigma}^{\rm dis}_{\rm OHE} + \bar{\sigma}^{\rm int}_{\rm OHE})$, where the bar denotes the absolute value and $\sigma_{\rm OHE}$ is computed numerically to access the full nonperturbative regime. For very strong scalar potentials (characteristic of vacancy defects [59]), we find that the OHE is essentially intrinsic provided $n \gtrsim 5\times 10^{12}\ \mathrm{cm}^{-2}$. Note that TMD devices operating in the metallic regime (with $\varepsilon \approx 1.1\,\Delta$ [66, 67]) have been demonstrated, so that pure intrinsic orbital transport

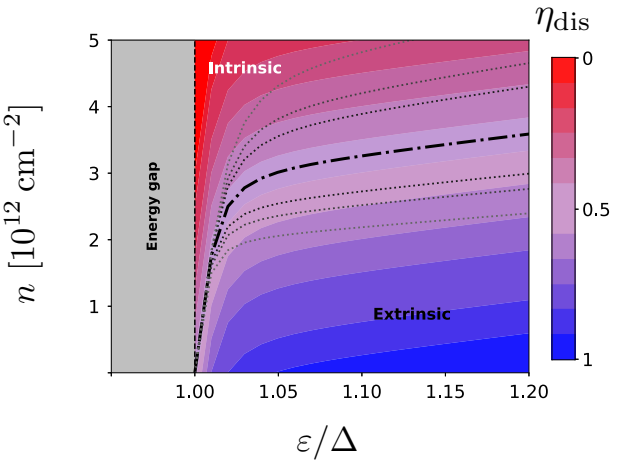

FIG. 3. Crossover between the intrinsic and extrinsic regimes of the OHE in a system with scalar disorder. The dash-dotted curve corresponds to the critical line $\eta_{\rm dis} = 1/2$ for impurities with $u_0 \equiv u_0^* = 100\,\mathrm{eVnm}^2$. The dotted lines show how the boundary changes upon tuning u_0. These transition from the left to the right of the u_0^* curve with u_0 increasing as $u_0/u_0^* = 0.67, 0.77, 0.83, 1, 1.2, 1.3, 1.5$. The color map represents the relative extrinsic contribution strength $\eta_{\rm dis} \in [0:1]$. Inside the energy gap, the OAM transport is governed by the orbital Berry curvature. Other parameters as in Fig. 2.

(that is, $\eta_{\rm dis} \ll 1$) may be within reach; see Fig. 3. We checked that the side-jump contribution to the OHC is typically too low to overcome intrinsic orbital transport, especially for strong scattering potentials [54]. Moreover, the extrinsic-to-intrinsic crossover is nonuniversal and smooth. Similarly to charge transport [68], the nature of OAM transport is sensitive to the carrier density and the details of the disorder model. As one moves away from the band edge into the metallic phase, the radius of the Fermi surface increases, which favors skew scattering processes. To better see this, in Fig. 3 we also show $n^* = n^*(\varepsilon, u_0)$, defined as the critical impurity density at which $\eta_{\rm dis} = 1/2$ and thus intrinsic and extrinsic mechanisms contribute equally. Below the critical n, the extrinsic OHC dominates. The family of dotted lines (which track the evolution of n^* with u_0) disclose a more prevailing extrinsic behavior of the OAM transport for weaker scattering potentials, as well as for higher carrier densities. In contrast, intrinsic orbital transport is seen to dominate close to the band edge and deep inside the dirty limit. Due to the prevalence of atomic defects in TMDs [65] with typical large $|u_0|$, these findings indicate that the two distinct OAM transport regimes should be accessible using a back-gate voltage. While this study is focused on zero-temperature properties, the general qualitative picture of the OHE remains the same at finite temperature, except for specific regions of the parameter space where electron-phonon scattering plays

a significant role (see Ref. [54] for additional details).

The problem of extrinsic OAM transport becomes even more intriguing when considering non-scalar disorder. Scattering potentials endowed with a nontrivial internal structure in the unit cell are ubiquitous but have so far not been investigated in the context of the OHE. For case (ii), in the limit of a pure staggered potential (see [54] for more general expressions), we find

$$\sigma_{\rm OHE}^{\rm s.c.(z)} = -\frac{2em_e v^2}{\pi n}\theta(|\varepsilon|-|\Delta|)\frac{\Delta}{u_z|\varepsilon|}\frac{f_1(\varepsilon,\Delta)}{f_2(\varepsilon,\Delta)} + \mathcal{O}(u_z^0). \tag{4}$$

For such impurities, the extrinsic OHC has instead even parity with respect to ε, which demonstrates that the *spatial symmetries* of local scattering potentials can have a large impact on the OHE. Note that the scaling with ε and Δ is also modified with respect to the case of scalar impurities [c.f. Eq. (3)]. This is interesting, but challenging to probe experimentally as *pure* staggered δ-type potentials are not easily accessible [55–57]. To see how the skewness of orbital scattering processes may vary between different types of common impurities, we investigate the OHC dependence on the ratio u_z/u_0. A representative study for $\varepsilon = 1.2\Delta$ is shown in the inset of Fig. 2. Upon increasing the staggered component of the potential, we see a quick reduction of the OHC from about $\approx 145\,(e/2\pi)$ at $u_z = 0$ (C_{6v}-symmetric impurities) to zero for $u_z = u_0$. The latter is the special case of short-ranged potentials localized on a single sublattice (C_{3v}-symmetric impurities), for which orbital skew scattering is conspicuously inactive. For $u_z > u_0$, the OHC changes sign and develops a nonmonotonic behavior, highlighting a subtle competition between orbital skew scattering processes of distinct origin. This confirms the intuition developed through Eqs. (3)-(4), that is, the structure of impurity potentials is key to developing a quantitative and qualitative description of extrinsic OAM transport.

Conclusion.—Taken together, our findings reveal a rich, hitherto unreported, interplay of OAM transport mechanisms that reflect the band structure and disorder landscape. In particular, we uncover an orbital analog of the familiar skew scattering mechanism, which is sensitive to the symmetry and strength of local impurity potentials. Despite our focus on 2D honeycomb layered systems with broken inversion symmetry, many of the OHE features we described here hold quite generally. Most importantly, the new orbital skew scattering mechanism is expected to be universal to orbital-active 2D electronic systems, both in the presence and absence of $\mathcal{T}$ symmetry. In particular, it will play a key role in centrosymmetric materials with hidden out-of-plane orbital textures, as shown in the Supplementary Material for the specific case of D_{6h}-invariant graphene with only intrinsic-type spin-orbit coupling [54]. The prevalent manifestation of orbital skew scattering is a crucial result and one of the main consequences of the microscopic OHE framework developed in this work.

T.G.R. acknowledges funding from the Portuguese Foundation for Science and Technology (FCT) through Grant Nos. 2022.07471.CEECIND/CP1718/CT0001 (with DOI identifier: 10.54499/2022.07471.CEECIND/CP1718/CT0001) 2023.11755.PEX, (with DOI identifier: https://doi.org/10.54499/2023.11755.PEX) and Strategic Funding UIDB/04650/2020. A.F. acknowledges partial support from the International Spintronics Network (Grant No. EP/V007211/1) funded by UK's Engineering and Physical Sciences Research Council (EPSRC). We thank the anonymous referees for valuable comments, which improved the Letter. A. F. further thanks Henrique P. V. C. Jorge for a close reading of the manuscript and for useful comments on the accuracy of the analytical approximations for the orbital Hall conductivity.

* aires.ferreira@york.ac.uk

[1] D. Go, D. Jo, H.-W. Lee, M. Kläui, and Y. Mokrousov, EPL (Europhysics Letters) **135**, 37001 (2021).
[2] S. Ding and et al., Phys. Rev. Lett. **125**, 177201 (2020).
[3] G. Sala and P. Gambardella, Phys. Rev. Res. **4**, 033037 (2022).
[4] D. Jo, D. Go, G.-M. Choi, and H.-W. Lee, npj Spintronics **2**, 19 (2024).
[5] H. Kontani, T. Tanaka, D. S. Hirashima, K. Yamada, and J. Inoue, Phys. Rev. Lett. **100**, 096601 (2008).
[6] D. Go, D. Jo, C. Kim, and H.-W. Lee, Phys. Rev. Lett. **121**, 086602 (2018).
[7] L. Salemi and P. M. Oppeneer, Phys. Rev. Mater. **6**, 095001 (2022).
[8] B. A. Bernevig, T. L. Hughes, and S.-C. Zhang, Phys. Rev. Lett. **95**, 066601 (2005).
[9] Y.-G. Choi, D. Jo, K.-H. Ko, D. Go, K.-H. Kim, H. G. Park, C. Kim, B.-C. Min, G.-M. Choi, and H.-W. Lee, Nature **619**, 52 (2023).
[10] I. Lyalin, S. Alikhah, M. Berritta, P. M. Oppeneer, and R. K. Kawakami, Phys. Rev. Lett. **131**, 156702 (2023).
[11] G. Sala, H. Wang, W. Legrand, and P. Gambardella, Phys. Rev. Lett. **131**, 156703 (2023).
[12] D. Go and H.-W. Lee, Phys. Rev. Res. **2**, 013177 (2020).
[13] D. Lee and et al., Nature Communications **12**, 6710 (2021).
[14] S. Ding, M.-G. Kang, W. Legrand, and P. Gambardella, Phys. Rev. Lett. **132**, 236702 (2024).
[15] S. Han, H.-W. Lee, and K.-W. Kim, Phys. Rev. Lett. **128**, 176601 (2022).
[16] O. Busch, F. Ziolkowski, B. Göbel, I. Mertig, and J. Henk, Phys. Rev. Res. **6**, 013208 (2024).
[17] T. S. Seifert and et al., Nature Nanotechnology **18**, 1132 (2023).
[18] S. Kumar and S. Kumar, Nature Communications **14**, 8185 (2023).
[19] Y. Xu and et al., Nature Communications **15**, 2043 (2024).

[20] D. Go and et al., "Orbital pumping by magnetization dynamics in ferromagnets," (2023), arXiv:2309.14817 [cond-mat.mes-hall].
[21] A. Manchon, A. Pezo, K.-W. Kim, and K.-J. Lee, "Orbital diffusion, polarization and swapping in centrosymmetric metals," (2023), arXiv:2310.04763 [cond-mat.mes-hall].
[22] S. Han and et al., Phys. Rev. Lett. **134**, 036305 (2025).
[23] E. Santos and et al., Phys. Rev. Appl. **19**, 014069 (2023).
[24] H. Hayashi, D. Go, S. Haku, Y. Mokrousov, and K. Ando, Nature Electronics **7**, 646–652 (2024).
[25] A. Johansson, B. Göbel, J. Henk, M. Bibes, and I. Mertig, Phys. Rev. Res. **3**, 013275 (2021).
[26] A. E. Hamdi and et al., Nature Physics **19**, 1855 (2023).
[27] P. Törmä, Phys. Rev. Lett. **131**, 240001 (2023).
[28] K. D. Belashchenko and et al., Phys. Rev. B **108**, 144433 (2023).
[29] M. Rang and P. J. Kelly, Phys. Rev. B **109**, 214427 (2024).
[30] J. Sohn, J. M. Lee, and H.-W. Lee, Phys. Rev. Lett. **132**, 246301 (2024).
[31] M. Offidani, M. Milletarì, R. Raimondi, and A. Ferreira, Phys. Rev. Lett. **119**, 196801 (2017).
[32] D. T. S. Perkins, A. Veneri, and A. Ferreira, Phys. Rev. B **109**, L241404 (2024).
[33] A. Pezo, D. García Ovalle, and A. Manchon, Phys. Rev. B **108**, 075427 (2023).
[34] H. Liu and D. Culcer, Phys. Rev. Lett. **132**, 186302 (2024).
[35] A. L. R. Barbosa, L. M. Canonico, J. H. García, and T. G. Rappoport, "Orbital hall effect and topology on a two-dimensional triangular lattice: from bulk to edge," (2023), arXiv:2311.11715 [cond-mat.mes-hall].
[36] P. Tang and G. E. W. Bauer, Phys. Rev. Lett. **133**, 186302 (2024).
[37] L. M. Canonico, J. H. Garcia, and S. Roche, Phys. Rev. B **110**, L140201 (2024).
[38] S. M. João, M. Anđelković, L. Covaci, T. G. Rappoport, J. M. V. P. Lopes, and A. Ferreira, Royal Society Open Science **7**, 191809 (2020).
[39] S. G. de Castro, J. M. V. P. Lopes, A. Ferreira, and D. A. Bahamon, Phys. Rev. Lett. **132**, 076302 (2024).
[40] L. M. Canonico, T. P. Cysne, T. G. Rappoport, and R. B. Muniz, Phys. Rev. B **101**, 075429 (2020).
[41] L. M. Canonico, T. P. Cysne, A. Molina-Sanchez, R. B. Muniz, and T. G. Rappoport, Phys. Rev. B **101**, 161409 (2020).
[42] S. Bhowal and S. Satpathy, Phys. Rev. B **102**, 035409 (2020).
[43] F. Xue, V. Amin, and P. M. Haney, Phys. Rev. B **102**, 161103 (2020).
[44] T. P. Cysne and et al., Phys. Rev. Lett. **126**, 056601 (2021).
[45] S. Bhowal and G. Vignale, Phys. Rev. B **103**, 195309 (2021).
[46] T. P. Cysne, S. Bhowal, G. Vignale, and T. G. Rappoport, Phys. Rev. B **105**, 195421 (2022).
[47] A. Pezo, D. García Ovalle, and A. Manchon, Phys. Rev. B **106**, 104414 (2022).
[48] T. P. Cysne, M. Costa, M. B. Nardelli, R. B. Muniz, and T. G. Rappoport, Phys. Rev. B **108**, 165415 (2023).
[49] O. Busch, I. Mertig, and B. Göbel, Phys. Rev. Res. **5**, 043052 (2023).
[50] M. Costa and et al., Phys. Rev. Lett. **130**, 116204 (2023).
[51] M. Milletarì and A. Ferreira, Phys. Rev. B **94**, 134202 (2016).
[52] C. Huang, Y. D. Chong, and M. A. Cazalilla, Phys. Rev. B **94**, 085414 (2016).
[53] M. Offidani and A. Ferreira, Phys. Rev. Lett. **121**, 126802 (2018).
[54] "See the Supplemental Material for (1) details on the diagrammatic method, including analytical expressions for the renormalized vertex and $\varrho(\varepsilon, \mathbf{k})$ in the weak and strong scattering regimes, (2) extrinsic OHC due to impurities admixing scalar and staggered potentials, (3) orbital side-jump correction, (4) orbital Hall angle, (5) finite-temperature studies and (6) extention of the theory to the Haldane and Kane-Mele models, which includes Refs. [69–74].".
[55] D. M. Basko, Phys. Rev. B **78**, 115432 (2008).
[56] C. Bena, Phys. Rev. Lett. **100**, 076601 (2008).
[57] A. Pachoud, A. Ferreira, B. Özyilmaz, and A. H. Castro Neto, Phys. Rev. B **90**, 035444 (2014).
[58] For group VI dichalcogenide monolayers, the picture is more involved due to the different sublattice and orbital content of the basis functions of the effective model.
[59] A. Ferreira and et al., Phys. Rev. B **83**, 165402 (2011).
[60] I. A. Ado, I. A. Dmitriev, P. M. Ostrovsky, and M. Titov, Europhysics Letters **111**, 37004 (2015).
[61] F. Joucken and et al., Nano Letters **21**, 7100 (2021).
[62] P. San-Jose, A. Gutiérrez-Rubio, M. Sturla, and F. Guinea, Phys. Rev. B **90**, 075428 (2014).
[63] J. Jung, A. M. DaSilva, A. H. MacDonald, and S. Adam, Nature Communications **6**, 6308 (2015).
[64] H. Qiu and et al., Nature Communications **4**, 2642 (2013).
[65] J. Hong and et al., Nature Communications **6**, 6293 (2015).
[66] B. Radisavljevic and A. Kis, Nature Materials **12**, 815 (2013).
[67] Z. Yu and et al., Nature Communications **5**, 5290 (2014).
[68] Significant weak localization effects occur when the mean free path approaches the Fermi wavelength, $l = v\tau_0 \lesssim \lambda_F$. Due to the Dirac nature of the spectrum, this regime is restricted to a narrow energy window for systems with strong impurities unless n is high (e.g. $\Delta < \epsilon \lesssim 1.1\Delta$ for $u_0 = u_0^*$ and $n \gtrsim 5 \times 10^{12}$ cm^{-2}).
[69] N. A. Sinitsyn, Q. Niu, and A. H. MacDonald, Phys. Rev. B **73**, 075318 (2006).
[70] N. M. R. Peres, Rev. Mod. Phys. **82**, 2673 (2010).
[71] S. Das Sarma, S. Adam, E. H. Hwang, and E. Rossi, Rev. Mod. Phys. **83**, 407 (2011).
[72] A. Kormányos and et al., 2D Materials **2**, 022001 (2015).
[73] K. Zollner, M. Gmitra, and J. Fabian, Phys. Rev. B **99**, 125151 (2019).
[74] D. Perkins and A. Ferreira, in *Encyclopedia of Condensed Matter Physics (Second Edition)*, edited by T. Chakraborty (Academic Press, Oxford, 2024) second edition ed., pp. 205–222.